Article

Crystallization and Texturing of $Sr_xBa_{1−x}Nb_2O_6$ Thin Films Prepared by Aqueous Solution Deposition—An *In Situ* X-ray Diffraction Study

Viviann Hole Pedersen, Anders Bank Blichfeld, Kristine Bakken, Dmitry Chernyshov, Tor Grande, and Mari-Ann Einarsrud*

ACCESS | Metrics & More | Article Recommendations | Supporting Information

ABSTRACT: Aqueous chemical solution deposition (CSD) is an environmentally friendly and highly flexible fabrication route to prepare oxide thin films. Here, we present an aqueous CSD process for ferroelectric $Sr_xBa_{1−x}Nb_2O_6$ (SBN) thin films on $SrTiO_3$ (STO) single-crystal substrates. *In situ* synchrotron X-ray diffraction was employed to study the crystallization of the films during thermal processing with heating rates in the range 0.04−20 °C/s. Three different crystal orientations of SBN were observed based on the heating rate and the orientation of the STO substrates. SBN(001) and SBN(310) orientations were observed on STO(100),

while only the SBN(311) orientation was observed on STO(110). The SBN(001) orientation was favored by an ultraslow heating rate of 0.04 °C/s, suggesting that this is the thermodynamic stable orientation. The SBN(310) orientation was kinetically favored at moderate heating rates and also promoted by increasing the Sr content in the film. A high heating rate of 20 °C/s rendered polycrystalline SBN films. It was revealed that nucleation and growth occurred via a classical Volmer−Weber (VW) growth mode and that the SBN grains preferably grow along the *c*-axis. The present findings demonstrate that control of nucleation and growth is a prerequisite to deposit films with different orientations and textures, which is detrimental for the film properties.
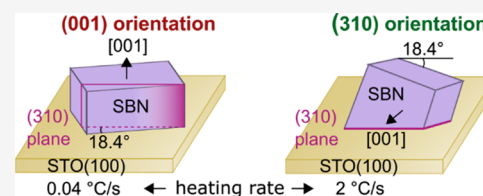
INTRODUCTION

Ferroelectric materials are important for the current development in electronics and smart sensors. They have a spontaneous and switchable polarization and are studied for their use in ferroelectric random-access memories, piezoelectric sensors and transducers, pyroelectric detectors, electro-optic modulators, and more.[1−3] Currently, the dominating materials used are lead zirconium titanate (PZT)-based, which contains about 60 wt % of toxic lead.[4−6] A big effort has therefore been placed on finding alternative lead-free ferroelectrics to replace PZT, and one option is the tetragonal tungsten bronze (TTB) $Sr_xBa_{1−x}Nb_2O_6$ (SBN) system.[4] SBN has shown good dielectric and electro-optic properties and a ferroelectric relaxor behavior for high Sr content ($x > 0.5$).[4,7−9] SBN has an unfilled TTB structure, giving an inherent disorder, great flexibility and tunable properties.[10−13] For example, changes in the Sr content (x) are known to change the ferroelectric properties, including the Curie temperature (T_C), which varies approximately linearly from 60 to 250 °C with increasing x in the range 0.25−0.75.[8] Furthermore, the ferroelectric polarization in SBN is uniaxial along the *c*-axis, making textured ceramics desirable to enhance the ferroelectric properties.[8,13]

Thin films offer advantages including texturing of the materials, improvement of properties, and potential minimization of devices.[14] For example, strain engineering with a proper choice of substrate and synthesis method can tune the properties of ferroelectric thin films.[14−16] SBN thin films

have been deposited by different synthesis methods, including PLD,[17−24] RF sputtering,[25−30] sol−gel synthesis,[31−39] polymeric chemical method,[40,41] and chemical solution deposition (CSD).[42] The physical deposition techniques are time-consuming, hard to upscale, or expensive, while wet chemical synthesis often uses toxic organic solvents. The focus for our group has therefore been to develop a wet chemical synthesis by an aqueous CSD as described in ref 42. The aqueous CSD method is a low-cost, flexible, and environmentally friendly deposition method.[43,44]

The structure of SBN thin films typically ranges from polycrystalline[40] to oriented and epitaxial,[21,23,35,36] where the type of substrate is an important parameter. Epitaxial or highly oriented growth has been reported on MgO,[26,28,30,31,36,45,46] $SrTiO_3$ (STO),[21,23,24,35,36] Si(100),[37,39] and $LaNiO_3/CeO_2/YSZ/Si(100)$.[20] The epitaxial orientation of SBN is mostly reported with the c-axis perpendicular to the substrate surface and with a rotation of 18.43° around the c-axis in SBN compared to the substrate.[21,23,46] There are two equivalent rotations, and a twin structure is often observed. In addition, particularly for TiO_2-terminated STO substrates, a different set

A

of orientations of SBN thin films are observed, the (310) and (130) equivalent orientations. These orientations have an in-plane polarization of SBN parallel to the substrate surface.[21,23,35,36] In addition to the substrate, the annealing temperature, heating, and cooling rates are expected to affect the SBN thin film formation and orientation.[37,45]

To control the crystallization and orientation of SBN thin films, knowledge of the mechanisms for nucleation, growth, and texture formation is essential. In this work, we investigate the effect of heating rate, substrate orientation, and composition on SBN thin film formation by an aqueous CSD route. The films were studied by *in situ* synchrotron X-ray diffraction (XRD) to reveal the crystallization and orientation of the films at different stages during heating, a technique not previously used for SBN thin films. Additionally, *ex situ* studies by scanning electron and atomic force microscopy were performed to correlate the findings to the microstructure. A nucleation and growth mechanism was proposed which enables tuning of the orientation of the thin films by controlling the heating rate, substrate orientation, and composition of the films.

■ EXPERIMENTAL SECTION

The Sr and Ba solutions were prepared according to the method presented by Raeder et al.[47] Ethylenediaminetetraacetic acid (EDTA, Sigma-Aldrich, >98.5%) and ammonia solution (NH_3(aq), AnalaR NORMAPUR, 28−30%) were added to deionized (DI) water and mixed at 60 °C until the solution turned clear. Barium nitrate ($Ba(NO_3)_2$, Sigma-Aldrich, 99.999%) or strontium nitrate ($Sr(NO_3)_2$, Sigma-Aldrich, 99.995%), dried at 200 °C, was then added together with citric acid (CA, Sigma-Aldrich, 99.0%) and stirred until completely dissolved. Finally, the pH was adjusted to 7 by ammonia solution. The concentration of Sr/Ba precursor solutions was 0.3 M, and the molar ratios of $Sr/Ba(NO_3)_2$/EDTA/NH_3(aq)/CA were 1:1:4.8:2.

Nb-acid ($Nb_2O_5 \cdot nH_2O$) was prepared according to the method presented by Madaro.[48] Ammonium niobate(V) oxalate hydrate (70 g, $NH_4NbO(C_2O_4)_2 \cdot H_2O$, Aldrich Chemistry, 99.99%) was dissolved in DI water (700 mL) at 60 °C before the pH was increased to 10−11 by adding ammonia solution (125 mL, 28−30%). The precipitated Nb-acid slurry was washed in ammonia solution (1 wt %) by centrifugation (10 000 rpm for 15 min) and decanting of the clear solution three times. A proper removal of residues of oxalates is important as both Sr- and Ba-oxalates are insoluble in water and would precipitate in the final SBN solution.[49] The Nb-acid slurry was then dispersed in a malic acid solution (MA, Sigma-Aldrich, ∼0.92 or 0.46 M) with a molar ratio Nb:MA of 1:2 by stirring at 80 °C until complete dissolution. Finally, the pH was adjusted to 7, and standardization was carried out by thermogravimetric analysis, which gave a Nb concentration of 0.2702 or 0.1427 M in the final precursor solution. Stable aqueous precursor solutions were made by mixing separate Sr, Ba, and Nb solutions in desired stoichiometric ratios. Three different compositions were used with Sr:Ba:Nb ratios of 40:60:190, 50:54.2:195, and 57.1:46.2:200, which are further referred to as SBN40, SBN50, and SBN57, respectively. All solutions, except the one used for the SBN40 film with a heating rate of 0.2 °C/s, had a Nb concentration of 0.184 M, while the mentioned solution had a Nb concentration of 0.0954 M.

The SBN precursor solution, filtered through a 0.2 μm filter, was deposited on O_2 plasma-cleaned substrates (Crystal GmbH, Germany, 10 × 10 × 0.5 mm³ STO(100) or STO(110) single crystals) by spin coating at 3500 rpm for 30 s. Following deposition, the films were dried at 200 °C on a hot plate for 4 min before crystallization by heating to 1000 °C using a heating rate of 0.04, 0.2, 2, or 20 °C/s and an annealing time of 25−60 min. Only one heating rate (2 °C/s) was used for the SBN40 and SBN50 composition prepared on STO(110), while all Sr:Ba ratios and heating rates were

used for SBN prepared on STO(100). *In situ* synchrotron XRD using a grazing incidence geometry with an incidence angle (ω) of 1−2° was performed during crystallization. An *in situ* rapid heating setup[42] was utilized for the *in situ* heating and XRD measurements. The setup consisted of a flat heating element (25 × 30 mm² active area, 850 W, Bach Resistor Ceramics GmbH) placed on a block of thermal insulation (Fiberfrax Duraboard). The insulation was attached to an outer alumina box which was connected to the beamline goniometer by goniometer connection. The samples were placed directly on the heating element and aligned to have the substrate edges parallel and perpendicular to the beam. This gave a substrate orientation where the [100] or [010] direction for STO(100) and the [001] or [$\bar{1}$10] direction for STO(110) was parallel with the beam direction. A thermocouple (type K) was used to monitor the surface temperature of the sample. The setup allowed heating rates up to 20 °C/s and a maximum surface temperature of 1100 °C.

To overcome the challenge of thermal expansion during heating, a height offset was imposed on the samples. The samples were continuously measured at repeating height offsets of 0, -100, −200, −300, and −400 μm, ensuring that at least one height had the sample inside the beam. The measurements were performed at BM01 at the Swiss-Norwegian beamlines (SNBL) at the European Synchrotron Radiation Facility (ESRF) in Grenoble. A beam size of 250 × 500 μm², a wavelength of 0.78006 or 0.78242 Å, and a two-dimensional (2D) detector (2M Pilatus) were used, taking advantage of the flexible infrastructure of the beamline.[50] All experiments were performed in ambient air and with a maximum surface temperature of 1000 °C. After cooling to room temperature (RT), additional measurement was carried out using two different detector heights to compensate for the detector gaps. Finally, omega scans were collected by varying the incidence angle between −1 and 20° to obtain texture information.

The X-ray wavelength and the detector position relative to the beam were determined by measuring an NIST SRM 660a LaB_6 standard and performing calibrations using the calibration module of pyFAI.[51] The integration of the data was performed using Bubble software[50] or the multigeometry module of pyFAI. Both full azimuth (η) angle integration to obtain one-dimensional (1D) data and sectioned integration with 5° section in η to obtain 2D data were performed. The 1D data were further adjusted for the sample height and thermal expansion by aligning the substrate peak with known thermal expansion. The 2D data were used in Rietveld refinements performed with MAUD (Materials Analysis Using Diffraction) software (v 2.92)[52] using the E-WIMV texture model to determine the texture orientation. Pole figures of the texture orientations were plotted using the MTEX toolbox in Matlab[53] using a reference orientation where the incoming beam is in the negative z-direction in the pole figures.

Selected films (SBN40 with a heating rate of 0.2 °C on STO(100)) were exposed to hydrothermal treatment in an SBN precursor suspension after complete crystallization. The SBN precursor suspension used was prepared by following the procedure described in ref 54 by taking the Nb-acid slurry, the intermediate product in making the Nb-acid, and mixing with ammonia solution (∼120−125 mL, 1 wt %), dried $Ba(NO_3)_2$, and $Sr(NO_3)_2$ in stoichiometric amounts to give SBN40. The Nb content corresponds to a Nb concentration of 0.5 M. The films were placed near the bottom of a Teflon-lined stainless-steel autoclave (20−24 mL) with a 70% filling factor of the SBN precursor suspension and heated to 250 °C for 48 h. After the hydrothermal treatment, the films were rinsed in DI water and dried vertically at 110 °C in air. A detailed account of the procedure has been reported here.[55]

The topography, substrate coverage, and thickness of the thin films were examined using a scanning electron microscopy (SEM APREO) and atomic force microscopy (AFM, Veeco diMultimode V) instrument. The AFM data were further analyzed using built-in functions in Gwyddion software.[56] The samples were placed with the sample edges aligned along with the image frame so that the <100> direction of the STO(100) substrate would point toward either edge of the images.
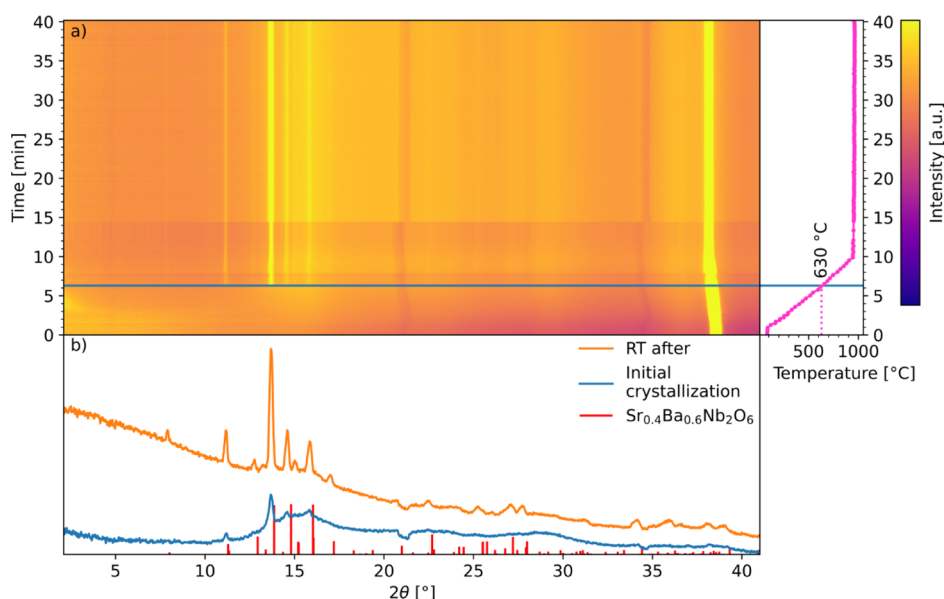
Figure 1. (a) 2D surface plot of integrated XRD diffractograms of the SBN40 film on STO(100) heated at 2 °C/s as a function of time/temperature. The time of the measurements is shown on the y-axis, while the corresponding temperature profile is displayed to the right. The intensity of the Bragg reflections is given by the color scale bar, and the blue line in the figure shows the initiation of the crystallization of the film. (b) Integrated XRD diffractogram from the initial crystalline frame in the film (blue) and the diffractogram taken after cooling to RT (orange). The red bars indicate where a diffraction line is expected in SBN40 crystals at RT based on Podlozhenov *et al.*[57]

Table 1. Crystallization Temperature, Texture Orientation Both Directly after the Initial Crystallization and after Cooling to RT, and the Degree of Texturing Observed at RT for the Different SBN Thin Films on STO(100) and STO(110) Substrates

composition [SBN%Sr]	heating rate [°C/s]	STO substrate orientation	crystallization temperature [°C][a]	texture orientation initial crystallization	final texture orientation	degree of texturing
	0.04	(100)	585 ± 1	(001)	(001)	highly textured
	0.2	(100)	611 ± 2	(001)	main: (001) minor: (310)	highly textured
SBN40	2	(100)	619−630[a]	(001)	main: (001) minor: (310)	highly textured
	20	(100)	625−724[a]	main: (310) minor: (001)		randomly oriented
	0.2	(100)	614 ± 2	(001)	main: (001) minor: (310)	highly textured
SBN50	2	(100)	619−626[a]	(001)	main: (001) minor: (310)	highly textured
	20	(100)	655−714[a]	main: (310) minor: (001)		randomly oriented
SBN57	2	(100)	622−631[a]	(001)	main: (001) minor: (310)	textured
	20	(100)	559−658[a]	(310)		randomly oriented
SBN40	2	(110)	628−645[a]	(311)	(311)	textured
SBN50	2	(110)	618−624[a]	(311)	(311)	textured

[a]For the medium and fast heating rates, a temperature interval is given for the crystallization temperature. The interval denotes the temperature of the last frame without any crystallization and the next frame where crystallization is visible. The temperature range could be as large as 100 °C for the fast heating rate (20 °C/s).

■ RESULTS

The crystallization process of the films upon heating was investigated by *in situ* XRD and summarized in 2D surface plots. Figure 1a shows the 2D plot of the SBN40 film with a heating rate of 2 °C/s on STO(100). The first appearance of diffraction lines defines the crystallization temperature and is marked by the blue line in Figure 1a. The crystallization temperature for the films is presented in Table 1 and was not observed to change with the Sr content and substrate orientation. The crystallization temperature of SBN was 585
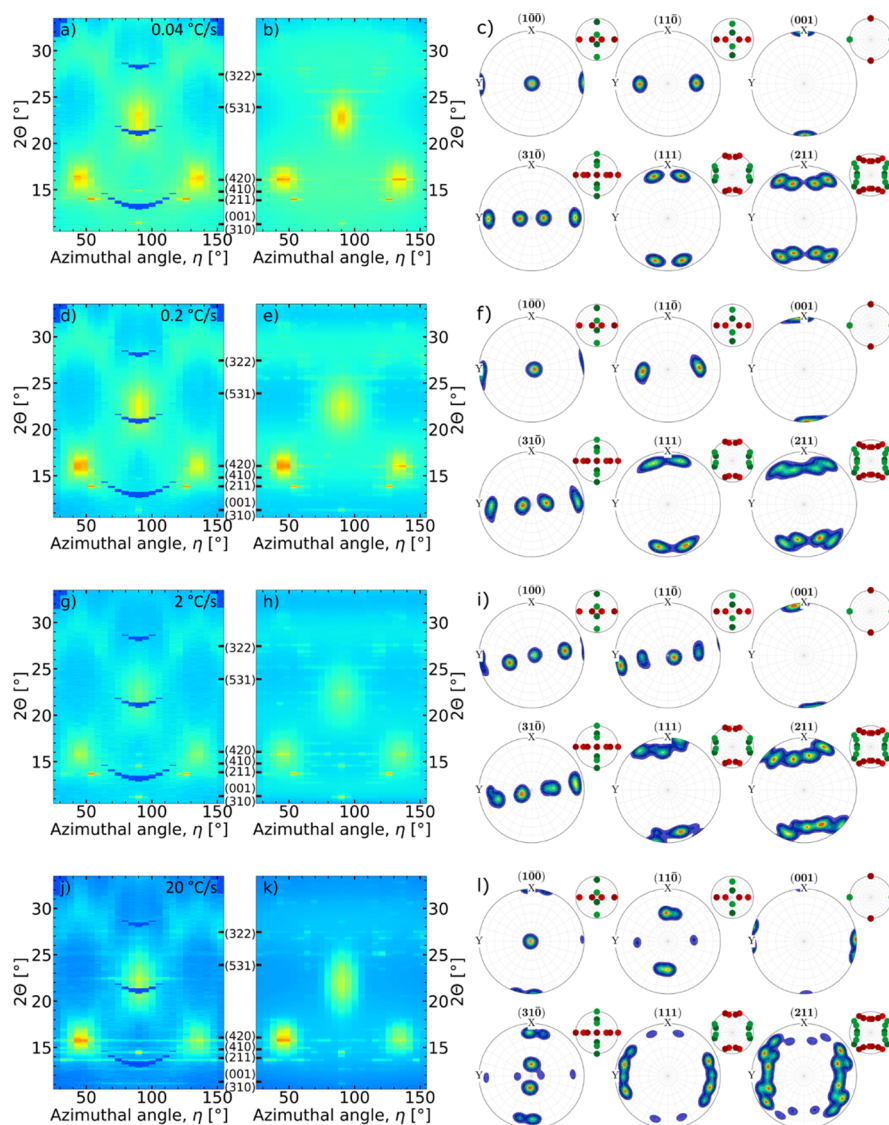
C

Figure 2. Experimental and calculated 2D XRD patterns and corresponding pole figure of the thin film orientations upon the initial crystallization for SBN40 films with a heating rate of 0.04−20 °C/s on STO(100) substrates. (a−c) 0.04 °C/s heating rate, (d−f) 0.2 °C/s heating rate, (g−i) 2 °C/s heating rate, and (j−l) 20 °C/s heating rate. (a,d,g,j) Experimental 2D XRD patterns for the film; (b,e,h,k) corresponding calculated patterns based on the Rietveld refinements with texturing. Relevant (hkl) reflections for SBN40 at RT are shown between the two 2D XRD patterns. (c,f,i,l) Pole figures for the orientations found in the refinements with the reference pole figure for the SBN(001) (red) and SBN(310) (green) orientation shown in the small circles to the upper right of each pole figure.

°C when an ultraslow heating rate (0.04 °C/s) was used, while increasing the heating rate caused a slight increase in the crystallization temperature. The crystallization temperature coincides well with 600 °C reported for SBN films prepared by nonaqueous sol−gel methods on Si substrates.[38] The trend is expected to be affected by the kinetics of the reaction; however, the increasing uncertainty in the crystallization temperature with increasing heating rate, caused by the increasing temperature interval between recorded frames, obscures the trend.

The films crystallized to single-phase SBN, and the lattice parameters remained stable after the initial crystallization. A small shift in the lattice parameters can be seen during heating due to thermal expansion which is most visible for the substrate diffraction line at 38°. The texture of the films was investigated at the initial crystallization and at RT after cooling, see selected diffractograms in Figure 1b. The composition of

the SBN films had a minimal effect on the texture and crystallinity. Therefore, mainly the data for the SBN40 films will be shown. The results for the SBN50 and SBN57 films are presented in Figures S1−S5 in the Supporting Information.

Thin films prepared with ultraslow to medium heating rates (0.04−2 °C/s) on STO(100) showed similar behavior upon the initial crystallization. The experimental and corresponding calculated diffraction data for the initial crystallization in the SBN40 films are shown in Figure 2, corresponding data for SBN50 and SBN57 are shown in Figures S1 and S4. To visualize the refined orientations, the orientation distribution function was extracted and used to plot the corresponding pole figures of the orientation, shown to the right in Figure 2. The thin films crystallized with the unique c-axis of the SBN crystal perpendicular to the substrate, in an SBN(001) orientation. This orientation is characterized by an out-of-plane orientation of the c-axis, and the a-axis rotated ±18.4° relative to the
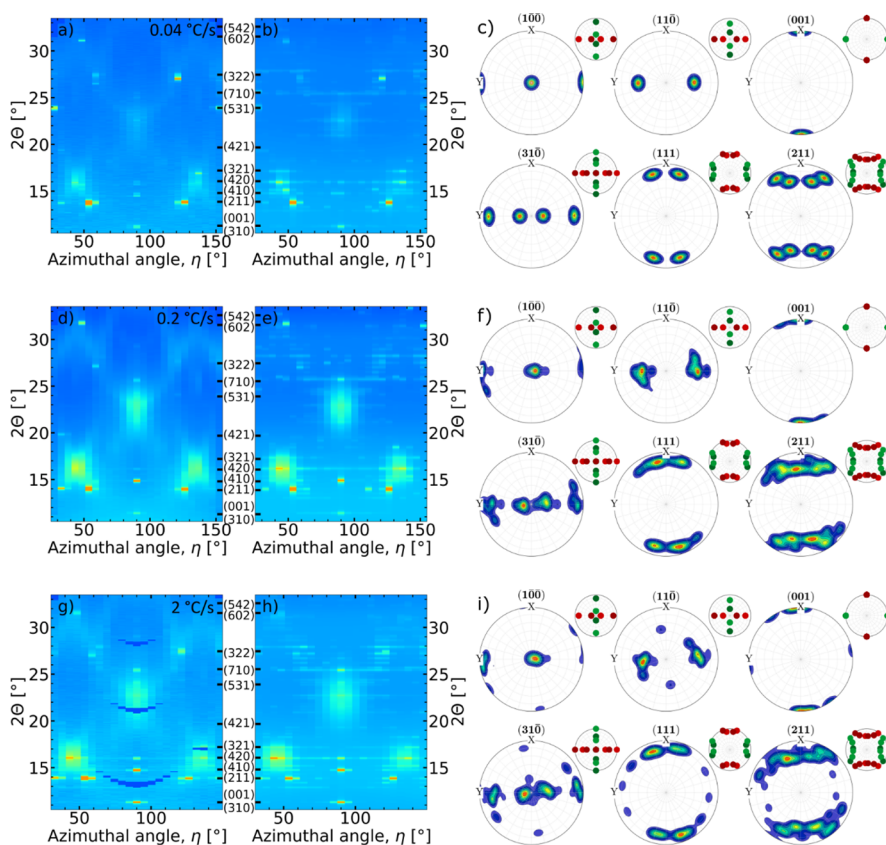
Figure 3. Experimental and calculated 2D XRD patterns and corresponding thin film orientations after cooling to RT for SBN40 films with a heating rate of 0.04−2 °C/s on STO(100) substrates. (a−c) 0.04 °C/s heating rate, (d−f) 0.2 °C/s heating rate, and 2 °C/s heating rate. (a,d,g) Experimental 2D XRD patterns for the film; (b,e,h) corresponding calculated patterns based on the Rietveld refinements with texturing. Relevant (hkl) reflections for SBN40 at RT are shown between the two 2D XRD patterns. (c,f,i) Pole figures for the orientation found in the refinements with the reference pole figure for the SBN(001) (red) and SBN(310) (green) orientation shown in the small circles to the upper right of each pole figure.
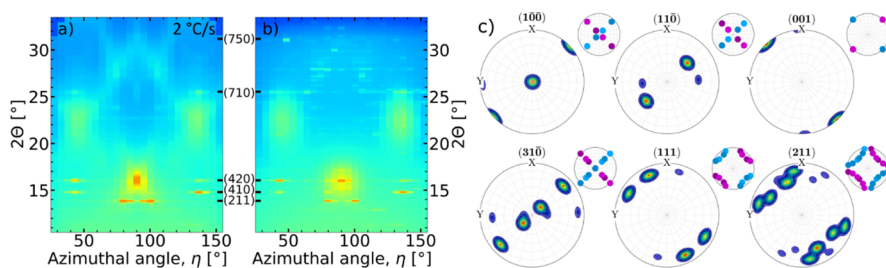

Figure 4. Experimental and calculated 2D XRD patterns and corresponding thin film orientations after cooling to RT for the SBN40 film with a heating rate of 2 °C/s on the STO(110) substrate. (a) Experimental 2D XRD pattern for the film and (b) corresponding calculated pattern based on the Rietveld refinements with texturing. Relevant (hkl) reflections for SBN40 at RT are shown between the two 2D XRD patterns. (c) Pole figures for the orientation found in the refinements with the reference pole figure for the (311) and (131) plane parallel to the substrate and with the c-axis of SBN pointing to the left (blue) or right (purple) shown in the small circles to the upper right of each pole figure.

<100> direction of STO, which corresponds to the {310} planes of SBN parallel to the <100> directions of the substrate.[21,23] For some of the films with heating rates of 0.2 and 2 °C/s, a second orientation with the c-axis and a {310} plane of SBN parallel to the substrate surface was observed, referred to as the SBN(310) orientation.[21,23,35,36] The amount of the second orientation was however too low for a Rietveld analysis. The fast heating rate films (20 °C/s), on the other hand, crystallized mainly in the SBN(310) orientation upon the initial crystallization. Some SBN(001) orientation was also observed in the SBN40 and SBN50 films, while for the SBN57

film, only the SBN(310) orientation was observed during the initial crystallization.

With prolonged crystallization time, the SBN(310) orientation became more prominent in all the films with heating rates of 0.2 and 2 °C/s. After cooling to RT, only the ultraslow heating rate film (0.04 °C/s) resulted in only SBN(001) orientation, as shown in Figure 3 for SBN40. The SBN(001) orientation was also dominant in the films prepared with heating rates of 0.2 and 2 °C/s, but the amount of crystals with SBN(310) orientation increased with increasing heating rate. For the fast heating rate (20 °C/s), the films were polycrystalline and no orientation was observed (not shown).
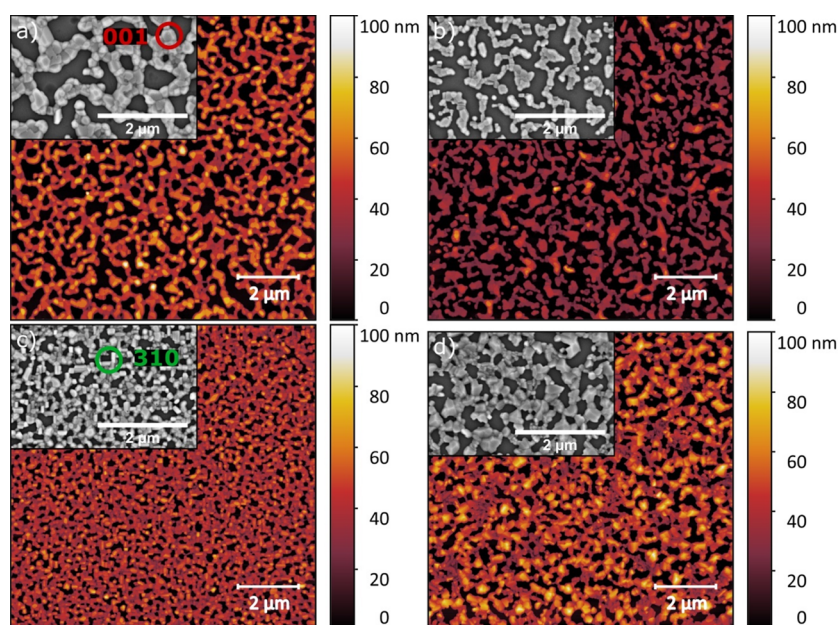
Figure 5. Topography AFM and SEM images showing the microstructure of the SBN40 thin films crystallized with a heating rate of (a) 0.04, (b) 0.2, (c) 2, and (d) 20 °C/s on STO(100). An overview of the samples is seen in the AFM image, while the insets are close-up SEM images. (a) Grains with an SBN(001) orientation which are cubes with a flat surface and a ±18.4° rotation compared to the image frame, highlighted by the red circle. (b,c) Grains with both the SBN(001) and SBN(310) orientations. The SBN(310) orientated grains are elongated squares with a pointed surface, due to a ±18.4° rotation around the *c*-axis of SBN, and with the elongated sides pointing directly at one of the image sides, highlighted by the green circle in (c). (d) Polycrystalline microstructure with several orientations of the grains.

The degree of texture in the films at RT depended on the heating rate. Slow heating rates (0.04 and 0.2 °C/s) resulted in highly textured films and middle heating rate (2 °C/s) resulted in textured films, while fast heating rate (20 °C/s) resulted in randomly oriented films. The degree of texture follows the same trend as seen for BTO deposited with CSD[58] and was best viewed from the omega scan data performed at RT, and these data are shown in Figures S6−S9 in the Supporting Information.

Thin films deposited on the STO(110) substrates displayed a different orientation than on STO(100). The resulting experimental and calculated data and the corresponding refined orientations for SBN40 are shown in Figure 4, and corresponding SBN50 data are shown in Figure S3. The substrate was oriented with the [001] direction parallel to the incoming beam. The SBN films were observed to have an orientation with one of the {311} planes parallel to the substrate surface, while one of the {310} planes intersected the substrate surface along the [001] direction of the substrate. This orientation will further be referred to as SBN(311) orientation.

The SBN thin film deposition resulted in partial coverage (51−81%) of the substrate with an average height of 29−45 nm and average lateral size in the range 130−175 nm. Topography images of the SBN40 films on STO(100) with a heating rate ranging from 0.04 to 20 °C/s are presented in Figure 5, and images of the SBN50 and SBN60 films are shown in Figure S10. The ultraslow heating rate (0.04 °C/s, Figure 5a) gave a lower coverage (63%) and a larger grain size (170 nm), while the 2 and 20 °C/s heating rates (Figure 5c,d) gave the highest coverage of 79 and 74% and a smaller grain size of 130 and 140 nm, respectively. The slow heating rate (0.2 °C/s, Figure 5b) stands out, giving the lowest coverage of 51% and an intermediate grain size of 155 nm. The low coverage is probably caused by the reduced concentration of the precursor solution for this sample. The SBN(001) and SBN(310) texture orientations are visible in the microstructure of the films and correspond well with previously reported microstructure for the two orientations in PLD-grown films.[23] Grains with the SBN(310) orientation consist of elongated rectangular squares which point toward one of the sides of the image, representing the <100> directions on the STO substrate. Each grain also has a pointed surface due to the ±18.4° rotation to cause the {310} plane to face the substrate surface. Grains with the SBN(001) orientation are cube-shaped or round with a flat surface and a slight rotation around the c-axis, again ±18.4° to make the {310} plane line up with the <100> direction in the STO substrate. Grains with the two orientations are highlighted in the inset of Figure 5a for the SBN(001) orientation by a red circle and Figure 5c for the SBN(310) orientation by a green circle. For the ultraslow heating rate (0.04 °C/s) film, only the SBN(001) orientation was observed in accordance with the XRD data. Furthermore, for the slow and medium heating rates (0.2 and 2 °C/s), both the SBN(001) and SBN(310) orientations were observed for the films. Finally, for the fast heating rate (20 °C/s), a mostly random orientation of the grains was observed corresponding to a polycrystalline film.

To further study the growth mechanism of SBN and increase the degree of film coverage on the substrates, selected films were placed in a suspension of SBN precursors and exposed to hydrothermal conditions. A topographic image of the SBN40 film on STO(100) heated at 2 °C/s before and after the hydrothermal treatment is shown in Figure 6. The hydrothermal treatment caused continued growth of SBN, revealing coarsened rectangular grains and preferable growth along the *c*-axis of SBN. The grain coarsening refers to the change in grain shape from more undefined to close to perfect rectangular shape and is expected to occur when the growth
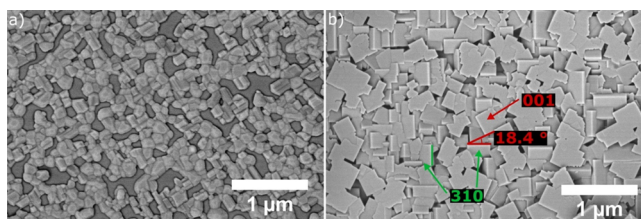
Figure 6. Topographic SEM image of the (a) SBN40 thin film with a heating rate of 2 °C/s on the STO(100) substrate before hydrothermal treatment and (b) hydrothermally treated SBN40 film. (b) Coarsened grains with sharp rectangular edges. The grains are rotated ±18.4° around the c-axis of SBN, as illustrated by the red angle for the SBN(001) oriented grains and green line for the SBN(310) oriented grains.

progresses mainly in kinks and steps on the surface, giving flat surfaces. Here, the ±18.4° rotation of both the SBN(001) and SBN(310) orientations is visible and highlighted in Figure 6 by the red angle for the SBN(001) orientation and the green line for the SBN(310) orientation. The SBN(310) orientation rotation is along the a- or b-axis of the substrate, making the sharp edges visible and marked by the green line. A more detailed report on the effect of hydrothermal treatment of SBN thin films, including a growth mechanism, can be found here.[55]

■ DISCUSSION

Texture Mechanism for SBN Thin Films on STO(100). The SBN thin films grown on STO(100) were observed with SBN(001) and SBN(310) orientations, as illustrated in Figure 7. Both orientations correspond to a family of planes in SBN aligning with a family of directions in STO, and the
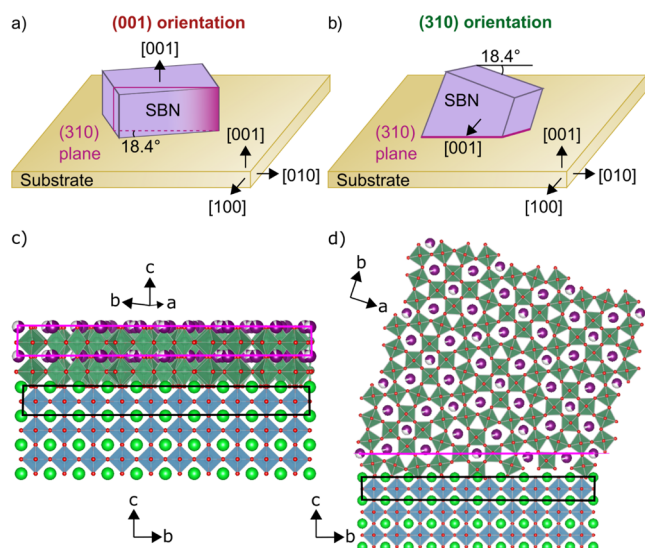

Figure 7. Illustration of (a) SBN(001) and (b) SBN(310) orientations on the STO(100) substrate. For the SBN(001) orientation, the c-axis of SBN is perpendicular to the STO substrate surface and the {310} planes are parallel to the [001] and [010] direction of STO. For the SBN(310) orientation, the c-axis of SBN is parallel to either the [100] or [010] direction of STO and one of the {310} planes in SBN is parallel to the substrate surface. The atomic interfaces between the (310) plane of SBN and the substrate surface is illustrated in (c) for the SBN(001) orientation and (d) for SBN(310) orientation, using 3 × 1 × 1 unit cells of SBN on top of 10 unit cells of STO.

orientations can therefore be achieved by several rotations of SBN on the substrate. For the SBN(001) orientation, SBN crystals are rotated ±18.4° around the c-axis of SBN, perpendicular to the substrate surface, creating twin boundaries between different grains. For the SBN(310) orientation, there is a ±18.4° rotation around the c-axis of SBN, parallel to the substrate surface, but here, the c-axis can also point in two equivalent directions, along the [100] or [010] direction of the substrate. The SBN(001) and SBN(310) orientations with their given rotations correspond to the six orientation modes presented by Su et al.[23] Su et al. further described a growth mechanism where the two orientations are expected to coexist in the thin film. The calculated lattice parameter mismatch between the two SBN orientations and the STO(100) substrate is summarized in Table 2. In the calculation, the minimum number of unit cells

Table 2. Calculated Lattice Mismatch for the SBN(001) and SBN(310) Orientations on the STO(100) Substrate and the SBN(311) Orientation on the STO(110) Substrate[a]

	STO(100)			STO(110)	
	lattice mismatch (001) orientation [%]	lattice mismatch (310) orientation [%]		lattice mismatch (311) orientation [%]	
composition					
SBN direction	$[1\bar{3}0]/[3\bar{1}0]$	$[001]$	$[1\bar{3}0]/[3\bar{1}0]$	$\sim[31\bar{1}0]$	$[1\bar{3}0]/[3\bar{1}0]$
SBN40	−1.09	−1.53	−1.09	−1.07	−1.09
SBN50	−1.00	−1.18	−1.00	−0.98	−1.00
SBN57	−0.92	−0.92	−0.92	−0.90	−0.92

[a]The lattice mismatches are calculated using the smallest repeating distance along the given direction of SBN and compared it to the closest whole number of STO unit cells along the [001] or [$\bar{1}$10] direction for STO(110).

needed to create a repeating lattice structure along the given SBN direction is used and compared to the closest number of unit cells of STO, illustrated in Figure 7c,d. In the calculation of the lattice mismatch, the two perpendicular directions in SBN along the substrate surface were considered separately. For the SBN(001) orientation, these two directions ([$1\bar{3}0$] or [$3\bar{1}0$]) are equivalent and have the same lattice mismatch. To represent SBN along the {310} planes, three unit cells were used and compared to 10 unit cells of STO along the <100> directions, illustrated in Figure 7c. For the SBN(310) orientation, one of the directions is equal to the SBN(001) orientation, see Figure 7d, while the other, [001] direction, will be the lattice mismatch between the c lattice parameter of SBN and the a lattice parameter of STO.

The calculated lattice mismatch for the SBN(001) and SBN(310) orientations combined with the observed orientations (Figures 2 and 3) suggests that the SBN(001) orientation is the thermodynamically most stable, while the SBN(310) orientation is kinetically favorable. To correlate the nucleation rate, of the expected heterogeneous nucleation, to the heating rate, one must consider that the temperature can both increase and decrease the nucleation rate, as the temperature affects both the supersaturation and the kinetics of the nucleation process.[59] A temperature window for nucleation is hence present, with a maximum nucleation rate at a certain temperature. From this, a fast heating rate is expected to drive the nucleation process to occur fast, as most nucleation will occur around the maximum rate. For a slower heating rate, the nucleation is expected to be slower, as more of the nucleus

formation is expected to occur before the maximum rate is reached. The nucleation rate will further influence the orientation of the nuclei on the substrate, where fast nucleation will give kinetically favored orientations, while slower heating rates favor the thermodynamically stable orientations.[59]

The SBN(310) orientation was not observed in the films prepared by ultraslow heating rate and became more significant with increasing heating rate, suggesting that it is favored when the kinetics control the nucleation and growth processes. Furthermore, a one-to-one unit cell relation exists between the c-axis of SBN and the <100> direction of STO for one of the perpendicular directions in the SBN(310) orientations. The one-to-one relationship is a simpler relation, involving fewer atoms, than aligning three unit cells of SBN to 10 unit cells of STO, which is the case for both directions in the SBN(001) orientation. The simplicity of the interface relation in one of the directions of SBN(310) orientation of SBN is also expected to favor the orientation kinetically. The SBN(001) orientation has a smaller lattice mismatch for the SBN40 and SBN50 compositions and an equal lattice mismatch for the SBN57 compared to the SBN(310) orientation. Furthermore, only an ultraslow heating rate gave films with only SBN(001) orientation at RT, indicating a thermodynamically favored orientation as the system has sufficient time to orient during the nucleation and growth. Finally, also the initial crystallization is expected to occur with the most stable SBN(001) orientation for all except the fastest heating rate as the nuclei can orientate before the starting temperature for nucleation is reached. This is also observed for all except the fastest heating rate of 20 °C/s. The reported orientation dependence on heating rate is not to the authors' knowledge been reported before.

The lattice mismatch between SBN and STO decreases with increasing Sr content, and the decrease is more significant for the SBN(310) orientation compared to the SBN(001) orientation, making an equal lattice mismatch for the two orientations for the SBN57 films. The change in lattice mismatch indicates that the stability of the orientations varies with Sr content and that the SBN(310) orientation could become thermodynamically most stable outside the studied composition range. No observation of the SBN(001) orientation in the SBN57 film with a heating rate of 20 °C/s supports this hypothesis. However, previous literature has reported SBN30-70 with (310) orientation by the nonaqueous sol−gel method[35] and (001) orientation for SBN50-60 by PLD,[24] indicating a dependency on the synthesis method and precursor chemistry.

SBN Thin Film Orientation on STO(110). SBN films grown on STO(110) substrates showed only the SBN(311) orientation. This SBN(311) orientation has four possible rotations which are equivalent in lattice mismatch. Both of the {311} planes, (311) and (131), could be parallel to the substrate surface, and correspondingly, the (310) or (130) planes will be parallel to the [001] direction of the substrate. Furthermore, as a plane should be parallel to a direction, the c-axis of SBN can point either to the left or to the right with a 180° rotation. One of the possible rotations of the SBN(311) orientations is illustrated in Figure 8, with the c-axis pointing to the right. To calculate the lattice mismatch between the SBN(311) orientation and the STO(110) substrate, the two perpendicular directions along the (311) plane were handled separately. For the direction along the [$1\bar{3}0$] or [$3\bar{1}0$] direction in SBN and the [001] direction of STO, the lattice mismatch is
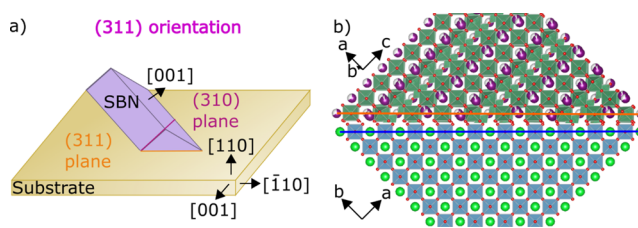

Figure 8. Illustration of (a) SBN(311) orientation on the STO(110) substrate and (b) corresponding atomic interface. The (311) plane of SBN (orange) is parallel to the (110) surface (blue) of the STO substrate and the (310) plane of SBN is parallel to the [001] direction of STO. (b) 3 × 1 × 10 unit cells of SBN on top of 10 unit cells of STO.

equal to the one given for the SBN(001) orientation on STO(100). For the perpendicular direction along the [$\bar{1}10$] direction of STO, illustrated in Figure 8b, there is no obvious point where the atomic structure along the direction repeats itself perfectly as the a and c lattice parameters are not a multiple of each other. Therefore, repetition was assumed when the plane spanned over three unit cells of SBN along the a-axis, which corresponds to almost 10 unit cell lengths along the c-axis. The length of this span is compared to 10 unit cells of STO along the [$\bar{1}10$] direction, giving the lattice mismatch included in Table 2.

Nucleation and Growth Mechanism for SBN Thin Film. The microstructure, including grain shape and substrate coverage, offers further insights into the growth mechanism of the SBN thin films. All grains are elongated along the c-axis, seen as an increased height for the SBN(001) grains and the rectangular shape of the SBN(310) grains (Figure 5). Based on this, the growth is expected to preferably, but not only, occur along the c-axis of SBN, as previously suggested.[21] Furthermore, the surface perpendicular to the c-axis is observed to be smooth, indicating that the growth primarily occurs in layers along the c-direction, as illustrated in Figure 9.
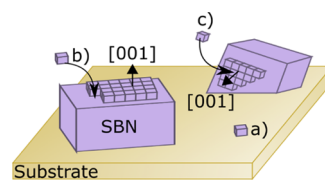

Figure 9. Schematic of the different steps of the proposed nucleation and growth for SBN thin films. (a) 2D nucleation on the substrate causing the formation of new SBN grains. (b) Growth of the SBN grains along the c-axis by layer-by-layer monomer integration. (c) 2D nucleation on the noncomplete SBN layer during growth.

However, most edges are rough or rounded which indicates that a new layer is initiated before the underlying one is complete, indicating that a 2D nucleation occurs on the growing SBN structure. The partial coverage of the thin films further shows that nucleation on SBN is favored over the STO substrate, creating islands instead of a homogeneous thin film. The proposed nucleation and growth mechanism for SBN thin films is therefore the classical Volmer−Weber (VW) growth mode, as previously suggested in the literature for PLD-grown SBN thin films.[30] However, other literature[23] studies suggest that the growth mode varies between VW and Frank−van Merwe depending on the growth conditions and precursors. Furthermore, the heating profile or pyrolysis temperature and

the precursor chemistry have been shown to be important for CSD thin films of BTO[58] and sol−gel films of PZT.[60] SBN is under the CSD precursor conditions expected to interact stronger with itself than with the STO substrate and give the previously described orientation dependence. The driving force for the 2D nucleation is a supersaturation of the solid solution on the substrate which is activated by the change in temperature. Furthermore, the initial orientation of the films remains throughout the film growth and in the RT data, see Table 1, suggesting that the nucleation and growth process occurs with limited reprecipitation of grain in different orientations. In addition, the second growth induced by hydrothermal conditions shows a coarsening of existing grains and no distinct formation of new grains, as seen from Figure 6. Finally, the SBN crystals were rectangular in shape, as the tetragonal crystal system of the material when given a prolonged time to grow. The final microstructure observed hence strengthens the proposed layer-by-layer growth mechanism.

Controlled Growth and Polarization of Textured SBN Thin Films. Knowledge about the texturing mechanism can be used to control the texture during film deposition. To achieve an SBN(001) orientated thin film, an ultraslow heating rate of 0.04 °C/s should be used. Furthermore, a low Sr content in the SBN is expected to ease the formation of the SBN(001) orientation. To obtain an SBN(310) oriented thin film, a moderate heating rate (around 2 °C/s) is recommended, and the process is facilitated using a higher Sr content in the SBN, as this reduces the lattice mismatch to the substrate. However, the current study was not able to achieve single-oriented SBN(310) thin films; hence, some additional measures are expected to be needed in this case. Furthermore, the lack of full coverage observed in the one-layer films studied here influences potential applications. An increased concentration of the precursor solution is expected to increase the film coverage, as the lowest film coverage was observed for the film with the lowest concentration (SBN40 film with 0.2 °C/s heating rate shown in Figure 5b). Adding additional deposition layers is also expected to increase the film coverage and film thickness. Finally, the introduction of a hydrothermal step for the crystallized films increased the coverage significantly and is a viable solution to improve film coverage and to increase the film thickness.

For practical application of the ferroelectric properties of the thin films, the orientation is important as SBN is a uniaxial ferroelectric with the polarization along the c-axis. Therefore, to achieve the highest polarizability of the films, it is desirable to have the uniaxial polarization pointing in the same direction for all grains in the textured films, making the SBN(001) orientation more desirable than both the SBN(310) and SBN(311) orientations. In the SBN(001) orientation, all polarization points perpendicular to the substrate surface, giving a single out-of-plane polarization. For the SBN(310) orientation, the polarization is in-plane, but as the grain can point in two directions, the maximum polarizability is reduced and the average polarization goes diagonally along the substrate surface. Finally, for the SBN(311) orientation, the c-axis has a 45° angle to the substrate surface and hence gives a mixture of out-of-plane and in-plane polarization which is usually undesirable. However, having an equal amount of the two 180° rotations can impose a net polarization either in-plane or out-of-plane depending on the poling direction.

CONCLUSIONS

An aqueous CSD route to prepare SBN thin films on STO single crystals is reported. The crystallization of the deposited films during thermal treatment, studied by *in situ* XRD, revealed the effect on the texturing of the thin films and the underlying nucleation and growth mechanism. SBN grown on STO(100) showed two orientations, SBN(001) and SBN(310), depending on the heating rate used for the synthesis, while SBN grown on STO(110) showed the SBN(311) orientation. The SBN(001) orientation is suggested to be the thermodynamically stable orientation, while the SBN(310) orientation is kinetically favored. Directions on how to promote the growth of the two different SBN orientations are given. The SBN(001) orientation is dominating at an ultraslow heating rate and low Sr content, while the SBN(310) orientation is preferred at a moderate heating rate and higher Sr content. The nucleation and growth mechanisms are based on the classical VW growth mode with 2D nucleation on both the substrate and the growing SBN crystals. SBN grains are further seen to preferably grow along the c-axis of SBN. The overall ferroelectric properties of the SBN thin films are highly dependent on the texture and preferable orientation of individual grains. The uniaxial nature of SBN makes it desirable with a single preferred orientation for the polarizable c-axis in SBN, which is only achieved in the SBN(001) orientation, making this favorable over the two other observed orientations SBN(310) and SBN(311).

ASSOCIATED CONTENT

Ⓢ Supporting Information

The Supporting Information is available free of charge at https://pubs.acs.org/doi/10.1021/acs.cgd.2c00553.

> Additional experimental data and details regarding 2D XRD patterns (SBN50 and SBN57 composition), Rietveld analysis, omega scans, and AFM analysis (PDF)

AUTHOR INFORMATION

Corresponding Author

Mari-Ann Einarsrud − *Department of Materials Science and Engineering, NTNU Norwegian University of Science and Technology, Trondheim 7491, Norway;* Ⓞ orcid.org/0000-0002-3017-1156; Email: mari-ann.einarsrud@ntnu.no

Authors

Viviann Hole Pedersen − *Department of Materials Science and Engineering, NTNU Norwegian University of Science and Technology, Trondheim 7491, Norway;* Ⓞ orcid.org/0000-0001-5526-9443

Anders Bank Blichfeld − *Department of Materials Science and Engineering, NTNU Norwegian University of Science and Technology, Trondheim 7491, Norway;* Present Address: Anders Bank Blichfeld, Danish Technological Institute, Gregersensvej 8, 2630 Taastrup, Denmark

Kristine Bakken − *Department of Materials Science and Engineering, NTNU Norwegian University of Science and Technology, Trondheim 7491, Norway;* Present Address: Kristine Bakken, Materials Center Leoben Forschung GmbH, Roseggerstrasse 12, 8700 Leoben, Austria.

Dmitry Chernyshov − *Swiss-Norwegian Beamlines, European Synchrotron Radiation Facility, Grenoble 38000, France;* orcid.org/0000-0001-7738-9358

Tor Grande − *Department of Materials Science and Engineering, NTNU Norwegian University of Science and Technology, Trondheim 7491, Norway*

Complete contact information is available at:
https://pubs.acs.org/10.1021/acs.cgd.2c00553

Author Contributions

Conceptualization, M.A.E, A.B.B, and TG.; methodology, A.B.B, M.A.E, and V.H.P.; investigation and data collection, A.B.B, B.K, and D.C; formal analysis, V.H.P with support from B.K and A.B.B.; writing-original draft preparation, V.H.P.; writing-review and editing, all authors; and funding acquisition, M.A.E and T.G. All authors have read and agreed to the published version of the manuscript.

Notes

The authors declare no competing financial interest.

■ ABBREVIATIONS

CSD   chemical solution deposition
SBN $Sr_xBa_{1-x}Nb_2O_6$
XRD   X-ray diffraction

■ REFERENCES

(1) Akasheh, F.; Myers, T.; Fraser, J. D.; Bose, S.; Bandyopadhyay, A. Development of piezoelectric micromachined ultrasonic transducers. *Sens. Actuators, A* **2004**, *111*, 275−287.

(2) Gupta, S.; Paliwal, A.; Gupta, V.; Tomar, M. Waveguide coupled surface plasmon resonance based electro optic modulation in SBN thin films. *Appl. Surf. Sci.* **2018**, *458*, 139−144.

(3) Kohli, M.; Wuethrich, C.; Brooks, K.; Willing, B.; Forster, M.; Muralt, P.; Setter, N.; Ryser, P. Pyroelectric thin-film sensor array. *Sens. Actuators, A* **1997**, *60*, 147−153.

(4) Shvartsman, V. V.; Lupascu, D. C. Lead-Free Relaxor Ferroelectrics. *J. Am. Ceram. Soc.* **2012**, *95*, 1−26.

(5) Liu, W.; Ren, X. Large Piezoelectric Effect in Pb-Free Ceramics. *Phys. Rev. Lett.* **2009**, *103*, 257602.

(6) Saito, Y.; Takao, H.; Tani, T.; Nonoyama, T.; Takatori, K.; Homma, T.; Nagaya, T.; Nakamura, M. Lead-free piezoceramics. *Nature* **2004**, *432*, 84−87.

(7) Lukasiewicz, T.; Swirkowicz, M. A.; Dec, J.; Hofman, W.; Szyrski, W. Strontium-barium niobate single crystals, growth and ferroelectric properties. *J. Cryst. Growth* **2008**, *310*, 1464−1469.

(8) Neurgaonkar, R. R.; Hall, W. F.; Oliver, J. R.; Ho, W. W.; Cory, W. K. Tungsten bronze $Sr_{1-x}Ba_xNb_2O_6$: A case history of versatility. *Ferroelectrics* **1988**, *87*, 167−179.

(9) Li, C.; Zhang, Y.; Liu, J.; Graetsch, H. A. Long-Range and Local Structure of $Sr_xBa_{1-x}Nb_2O_6$ (x = 0.33 and 0.67) across the Ferroelectric-Relaxor Transition. *Chem. Mater.* **2020**, *32*, 1844−1853.

(10) Jamieson, P. B.; Abrahams, S. C.; Bernstein, J. L. Ferroelectric Tungsten Bronze-Type Crystal Structures. I. Barium Strontium Niobate $Ba_{0.27}Sr_{0.75}Nb_2O_5$.78. *J. Chem. Phys.* **1968**, *48*, 5048−5057.

(11) Paściak, M.; Ondrejkovic, P.; Kulda, J.; Vaněk, P.; Drahokoupil, J.; Steciuk, G.; Palatinus, L.; Welberry, T. R.; Fischer, H. E.; Hlinka, J.; Buixaderas, E. Local structure of relaxor ferroelectric $Sr_xBa_{1-x}Nb_2O_6$ from a pair distribution function analysis. *Phys. Rev. B* **2019**, *99*, 104102.

(12) Kleemann, W. The relaxor enigma - charge disorder and random fields in ferroelectrics. *J. Mater. Sci.* **2006**, *41*, 129−136.

(13) Oliver, J. R.; Neurgaonkar, R. R.; Cross, L. E. A thermodynamic phenomenology for ferroelectric tungsten bronze $Sr_{0.6}Ba_{0.4}Nb_2O_6$(SBN:60). *J. Appl. Phys.* **1988**, *64*, 37−47.

(14) Cruz, J. P. d. l; Joanni, E.; Vilarinho, P. M.; Kholkin, A. L. Thickness effect on the dielectric, ferroelectric, and piezoelectric properties of ferroelectric lead zirconate titanate thin films. *J. Appl. Phys.* **2010**, *108*, 114106.

(15) Damodaran, A. R.; Agar, J. C.; Pandya, S.; Chen, Z.; Dedon, L.; Xu, R.; Apgar, B.; Saremi, S.; Martin, L. W. New modalities of strain-control of ferroelectric thin films. *J. Phys.: Condens. Matter* **2016**, *28*, 263001.

(16) Schlom, D. G.; Chen, L.-Q.; Fennie, C. J.; Gopalan, V.; Muller, D. A.; Pan, X.; Ramesh, R.; Uecker, R. Elastic strain engineering of ferroic oxides. *MRS Bull.* **2014**, *39*, 118−130.

(17) Gupta, S.; Paliwal, A.; Gupta, V.; Tomar, M. Study of ferroelectric SBN thin films for electro-optic applications. *2016 Joint IEEE International Symposium on the Applications of Ferroelectrics, European Conference on Application of Polar Dielectrics, and Piezoelectric Force Microscopy Workshop (ISAF/ECAPD/PFM). 21-25 Aug. 2016,* 2016; pp 1−3.

(18) Gupta, S.; Kumar, A.; Gupta, V.; Tomar, M. Electrical properties of Strontium Barium Niobate ($Sr_{0.6}Ba_{0.4}Nb_2O_6$) thin films deposited by pulsed laser deposition technique. *Vacuum* **2019**, *160*, 434−439.

(19) Cheng, H.-F.; Chiou, G.-S.; Liu, K.-S.; Lin, I. N. Ferroelectric properties of $(Sr_{0.5}Ba_{0.5})Nb_2O_6$ thin films synthesized by pulsed laser deposition. *Appl. Surf. Sci.* **1997**, *113-114*, 217−221.

(20) Chiu, T.-W.; Wakiya, N.; Shinozaki, K.; Mizutani, N. Growth of highly (001)-textured strontium barium niobate thin films on epitaxial $LaNiO_3/CeO_2/YSZ/Si(100)$. *Thin Solid Films* **2003**, *426*, 62−67.

(21) Infortuna, A.; Muralt, P.; Cantoni, M.; Setter, N. Epitaxial growth of $(SrBa)Nb_2O_6$ thin films on $SrTiO_3$ single crystal substrate. *J. Appl. Phys.* **2006**, *100*, 104110.

(22) Willmott, P. R.; Herger, R.; Patterson, B. D.; Windiks, R. Experimental and theoretical study of the strong dependence of the microstructural properties ofSrxBa1−xNb2O6thin films as a function of their composition. *Phys. Rev. B* **2005**, *71*, 144114.

(23) Su, D.; Infortuna, A.; Muralt, P.; Setter, N.; Cantoni, M. Transmission-electron-microscopy study of quasi-epitaxial tungsten-bronze $(Sr_{2.5}Ba_{2.5}Nb_{10}O_{30})$ thin film on perovskite $(SrTiO_3)$ single crystal. *J. Mater. Res.* **2007**, *22*, 157−163.

(24) Infortuna, A.; Muralt, P.; Cantoni, M.; Tagantsev, A.; Setter, N. Microstructural and electrical properties of $(Sr,Ba)Nb_2O_6$ thin films grown by pulsed laser deposition. *J. Eur. Ceram. Soc.* **2004**, *24*, 1573−1577.

(25) Hung, H.-F.; Yang, C.-F.; Wu, C.-C. Electrical Properties of Nanocrystalline Strontium Barium Niobate Thin Films Deposited at Room Temperature. *Sensor. Mater.* **2017**, *29*, 397−404.

(26) Cuniot-Ponsard, M.; Desvignes, J.; Ea-Kim, B.; Rodier, J.-C.; Leroy, E.., Growth of strontium barium niobate thin films (SBN:x) for nonlinear optics applications. *Applications of Photonic Technology 5*; SPIE, 2003; Vol. *4833*.

(27) Cuniot-Ponsard, M.; Desvignes, J. M.; Bellemain, A.; Bridou, F. Simultaneous characterization of the electro-optic, converse-piezo-electric, and electroabsorptive effects in epitaxial $(Sr,Ba)Nb_2O_6$ thin films. *J. Appl. Phys.* **2011**, *109*, 014107.

(28) Pavlenko, A. V.; Zakharchenko, I. N.; Kudryavtsev, Y. A.; Kiseleva, L. I.; Alikhadzhiev, S. K. Structural Characteristics of Thin

$Sr_{0.5}Ba_{0.5}Nb_2O_6$ Films in the Temperature Range 20-500°C. *Inorg. Mater.* **2020**, *56*, 1188−1192.

(29) Pavlenko, A. V.; Kiselev, D. A.; Matyash, Y. Y. DielectricFerroelectric Properties of Thin Heteroepitaxial Films of SBN-50. *Phys. Solid State* **2021** DOI: 10.1134/s1063783421060160.

(30) Stryukov, D. V.; Zinchenko, S. P.; Nazarenko, A. V.; Pavlenko, A. V. Influence of the sputtering conditions on the microstructure and lattice constants of $Sr_{0.5}Ba_{0.5}Nb_2O_6$ heteroepitaxial thin films. *Ferroelectrics* **2021**, *576*, 129−135.

(31) Koo, J.; Jang, J. H.; Bae, B.-S. Crystallization Behavior of Sol-Gel-Derived Strontium Barium Niobate Thin Films. *J. Am. Ceram. Soc.* **2001**, *84*, 193−199.

(32) Shen, Z.; Ye, H.; Zou, T.; Guo, B. Preparation and properties of highly c-axis-oriented $Sr_{0.6}Ba_{0.4}Nb_2O_6$ thin films by the sol-gel process. *Proceedings, Optoelectronic Devices and Integration*, 2005; Vol. 5644.

(33) Sakamoto, W.; Yogo, T.; Kikuta, K.; Ogiso, K.-j.; Kawase, A.; Hirano, S.-i. Synthesis of Strontium Barium Niobate Thin Films through Metal Alkoxide. *J. Am. Ceram. Soc.* **1996**, *79*, 2283−2288.

(34) Xu, Y.; Chen, C. J.; Xu, R.; Mackenzie, J. D. Ferroelectric $Sr_{0.60}Ba_{0.40}Nb_2O_6$ thin films by the sol-gel process: Electrical and optical properties. *Phys. Rev. B: Condens. Matter Mater. Phys.* **1991**, *44*, 35−41.

(35) Nishio, K.; Watanabe, Y.; Tsuchiya, T. Epitaxial Growth of $Sr_xBa_{1-x}Nb_2O_6$ Thin Films Prepared from Sol-Gel Process. *J. Sol-Gel Sci. Technol.* **2003**, *26*, 245−250.

(36) Nishio, K.; Seki, N.; Thongrueng, J.; Watanabe, Y.; Tsuchiya, T. Preparation and Properties of Highly Oriented $Sr_{0.3}Ba_{0.7}Nb_2O_6$ Thin Films by a Sol-Gel Process. *J. Sol-Gel Sci. Technol.* **1999**, *16*, 37−45.

(37) Shen, Z.; Xiao-Yan, C.; Ye, H.; Deng, N.-H.; Guo, B. Gu-Rerost, Growth of highly c-axis oriented SBN thin films on Si(100) with/without MgO buffer layer by the sol-gel method*. *J. Mater. Sci.* **2004**, *39*, 6871−6873.

(38) Ho, M. M. T.; Tang, T. B.; Mak, C. L.; Pang, G. K. H.; Chan, K. Y.; Wong, K. H. Spectroellipsometric studies of sol-gel derived $Sr_{0.6}Ba_{0.4}Nb_2O_6$ films. *J. Appl. Phys.* **2006**, *100*, 083524.

(39) Shen, Z.; Ye, H.; Mak, C. L.; Wong, K. H.; Yum, T. Y.; Liu, W.; Zou, T. Preparation of highly c-axis oriented $Sr_{0.6}Ba_{0.4}Nb_2O_6$ thin films grown on Silicon substrate by the sol-gel process. *Mater. Chem. Phys.* **2006**, *99*, 10−14.

(40) Melo, M.; Araujo, E. B.; Turygin, A. P.; Shur, V. Y.; Kholkin, A. L. Physical properties of strontium barium niobate thin films prepared by polymeric chemical method. *Ferroelectrics* **2016**, *496*, 177−186.

(41) Mendes, R. G.; Araujo, E.; Klein, H.; Eiras, J. B Cerámica y Vidrio Synthesis and characterization of Strontium Barium Niobate (SBN) ferroelectric thin films. *Bol. Soc. Esp. Ceram. Vidrio* **1999**, *38*, 455−457.

(42) Blichfeld, A. B.; Bakken, K.; Chernyshov, D.; Glaum, J.; Grande, T.; Einarsrud, M.-A. Experimental setup for high-temperature in situ studies of crystallization of thin films with atmosphere control. *J. Synchrotron Radiat.* **2020**, *27*, 1209−1217.

(43) Bassiri-Gharb, N.; Bastanib, Y.; Bernalc, A. Chemical solution growth of ferroelectric oxide thin films and nanostructures. *Chem. Soc. Rev.* **2014**, *43*, 2125−2140.

(44) Schwartz, R. W.; Schneller, T.; Waser, R. Chemical solution deposition of electronic oxide films. *C. R. Chim.* **2004**, *7*, 433−461.

(45) Zhu, J.; Singh, S. K.; Thomas, P. A.; Palmer, S. B. Crystalline Properties of Strontium Barium Niobate Thin Films Produced by Pulsed Laser Deposition. *Cryst. Res. Technol.* **1999**, *34*, 1205−1211.

(46) Willmott, P. R.; Herger, R.; Patterson, B. D.; Windiks, R. Experimental and theoretical study of the strong dependence of the microstructural properties of $Sr_xBa_{1-x}Nb_2O_6$ thin films as a function of their composition. *Phys. Rev. B* **2005**, *71*, 144114.

(47) Raeder, T. M.; Bakken, K.; Glaum, J.; Einarsrud, M. A.; Grande, T. Enhanced in-plane ferroelectricity in $BaTiO_3$ thin films fabricated by aqueous chemical solution deposition. *AIP Adv.* **2018**, *8*, 105228.

(48) Madaro, F. *Synthesis of Textured $K_xNa_{1-x}NbO_3$ Materials*; Norwegian University of Science and Technology: NTNU. Trondheim, Norway, 2010.

(49) Physical Constants of Inorganic Compounds. *CRC Handbook of Chemistry and Physics*; Rumble, J. R., Ed.; CRC Press/Taylor & Francis: Boca Raton, FL; Vol. 103, (Internet Version 2022).

(50) Dyadkin, V.; Pattison, P.; Dmitriev, V.; Chernyshov, D. A new multipurpose diffractometer PILATUS@SNBL. *J. Synchrotron Radiat.* **2016**, *23*, 825−829.

(51) Ashiotis, G.; Deschildre, A.; Nawaz, Z.; Wright, J. P.; Karkoulis, D.; Picca, F. E.; Kieffer, J. The fast azimuthal integration Python library:pyFAI. *J. Appl. Crystallogr.* **2015**, *48*, 510−519.

(52) Lutterotti, L. Total pattern fitting for the combined size−strain−stress−texture determination in thin film diffraction. *Nucl. Instrum. Methods Phys. Res. Sect. B Beam Interact. Mater. Atoms* **2010**, *268*, 334−340.

(53) Bachmann, F.; Hielscher, R.; Schaeben, H. Texture Analysis with MTEX - Free and Open Source Software Toolbox. *Solid State Phenom.* **2010**, *160*, 63−68.

(54) Grendal, O. G.; Blichfeld, A. B.; Vu, T. D.; van Beek, W.; Selbach, S. M.; Grande, T.; Einarsrud, M.-A. Composition and morphology tuning during hydrothermal synthesis of $Sr_xBa_{1-x}Nb_2O6$ tetragonal tungsten bronzes studied by in situ X-ray diffraction. *CrystEngComm* **2019**, *21*, 5922−5930.

(55) Hole, V. *Hydrothermal Synthesis of $Sr_xBa_{1-x}Nb_2O_6$ on Nanostructured Substrates*; Norwegian University of Science and Technology, 2019.NTNU Open

(56) Nečas, D.; Klapetek, P. Gwyddion: an open-source software for SPM data analysis. *Open Phys.* **2012**, *10*, 181−188.

(57) Podlozhenov, S.; Graetsch, H. A.; Schneider, J.; Ulex, M.; Wöhlecke, M.; Betzler, K. Structure of strontium barium niobate $Sr_xBa_{1-x}Nb_2O_6$ (SBN) in the composition range 0.32 ≤ x ≤ 0.82. *Acta Crystallogr. B* **2006**, *62*, 960−965.

(58) Bakken, K.; Blichfeld, A. B.; Chernyshov, D.; Grande, T.; Glaum, J.; Einarsrud, M.-A. Mechanisms for texture in $BaTiO3$ thin films from aqueous chemical solution deposition. *J. Sol-Gel Sci. Technol.* **2020**, *95*, 562−572.

(59) De Yoreo, J. J.; Vekilov, P. G. Principles of Crystal Nucleation and Growth. *Rev. Mineral. Geochem.* **2003**, *54*, 57−93.

(60) Fè, L.; Norga, G. J.; Wouters, D. J.; Maes, H. E.; Maes, G. Chemical structure evolution and orientation selection in sol-gel-prepared ferroelectric $Pb(Zr,Ti)O_3$ thin films. *J. Mater. Res.* **2001**, *16*, 2499−2504.

K